Efficient wide-bandgap perovskite solar cells with open-circuit voltage deficit below 0.4 V via hole-selective interface engineering

SCIENCE CHINA
Chemistry

•ARTICLES•

June 2024 Vol.67 No.6: 2102–2110
https://doi.org/10.1007/s11426-023-1966-1

Efficient wide-bandgap perovskite solar cells with open-circuit voltage deficit below 0.4 V *via* hole-selective interface engineering

Xiaoyu Ji[1†], Shuo Zhang[1†], Furong Yu[1], Huidong Zhang[1], Liqing Zhan[1], Yue Hu[2], Wei-Hong Zhu[1] & Yongzhen Wu[1*]

[1]*Key Laboratory for Advanced Materials and Joint International Research Laboratory of Precision Chemistry and Molecular Engineering, Shanghai Key Laboratory of Functional Materials Chemistry, Frontiers Science Center for Materiobiology and Dynamic Chemistry, Institute of Fine Chemicals, School of Chemistry and Molecular Engineering, East China University of Science and Technology, Shanghai 200237, China;*
[2]*School of Chemistry, University of Edinburgh, King's Buildings, Edinburgh EH9 3FJ, UK*

Received November 20, 2023; accepted February 13, 2024; published online May 21, 2024

Wide-bandgap mixed-halide perovskite solar cells (WBG-PSCs) are promising top cells for efficient tandem photovoltaics to achieve high power conversion efficiency (PCE) at low cost. However, the open-circuit voltage (V_{OC}) of WBG-PSCs is still unsatisfactory as the V_{OC}-deficit is generally larger than 0.45 V. Herein, we report a buried interface engineering strategy that substantially improves the V_{OC} of WBG-PSCs by inserting amphiphilic molecular hole-selective materials featuring with a cyanovinyl phosphonic acid (CPA) anchoring group between the perovskite and substrate. The assembly and redistribution of CPA-based amphiphilic molecules at the perovskite-substrate buried interface not only promotes the growth of a low-defect crystalline perovskite thin film, but also suppresses the photo-induced halide phase separation. The energy level alignment between wide-bandgap perovskite and the hole-selective layer is further improved by modulating the substituents on the triphenylamine donor moiety (methoxyls for MPA-CPA, methyls for MePA-CPA, and bare TPA-CPA). Using a 1.68 eV bandgap perovskite, the MePA-CPA-based devices achieved an unprecedentedly high V_{OC} of 1.29 V and PCE of 22.3% under standard AM 1.5 sunlight. The V_{OC}-deficit (<0.40 V) is the lowest value reported for WBG-PSCs. This work not only provides an effective approach to decreasing the V_{OC}-deficit of WBG-PSCs, but also confirms the importance of energy level alignment at the charge-selective layers in PSCs.

cyanovinyl phosphonic acid, energy level alignment, hole-selective material, open-circuit voltage, wide-bandgap perovskite

Citation: Ji X, Zhang S, Yu F, Zhang H, Zhan L, Hu Y, Zhu W, Wu Y. Efficient wide-bandgap perovskite solar cells with open-circuit voltage deficit below 0.4 V *via* hole-selective interface engineering. *Sci China Chem*, 2024, 67: 2102–2110, https://doi.org/10.1007/s11426-023-1966-1

1 Introduction

Single-junction perovskite solar cells (PSCs) have made unprecedented progress in recent years, with power conversion efficiency (PCE) record over 26% [1,2]. Thanks to their tunable bandgap (E_g) and facile fabrication, PSCs are also promising candidates for constructing tandem solar cells that are capable of further boosting the PCE and breaking the Schockley-Queisser (SQ) limit of single-junction devices [3–5]. A highly efficient wide-bandgap PSC (WBG-PSC) is essential for tandems. However, currently most WBG-PSCs (E_g > 1.65 eV) suffer from large open-circuit voltage (V_{OC}) losses, which restricts the tandem solar cells to approach their efficiency limit [6–11]. The large V_{OC}-deficit ($E_g/q - V_{OC}$) of WBG-PSCs is mainly correlated with the non-radiative recombination induced by the interfacial and bulk defects in polycrystalline perovskites, and the energy level

†These authors contributed equally to this work.
*Corresponding author (email: wu.yongzhen@ecust.edu.cn)

mismatch between the perovskite and charge-selective layers [10,12–17]. Accordingly, tremendous efforts have been devoted to decreasing the V_{OC}-deficit, including composition engineering [18–20], defect passivation [7,21–24], and development of novel charge-selective materials for improving interfacial band alignment [25–27]. However, V_{OC}-deficit is still generally larger than 0.45 V. To further minimize the V_{OC}-deficit of WBG-PSCs, novel materials should be developed addressing the issues of WBG-PSCs.

The WBG-PSCs in tandems are almost exclusively based on an inverted (p-i-n) device configuration due to their thin charge-selective layers (nm to tens of nm) and low-temperature fabrication (below 100 °C) [4,27]. In a p-i-n configuration, the perovskite is deposited on top of the hole-selective layer (HSL), and thus the properties of HSL play a vital role in the crystallization process of perovskite absorber [27]. An ideal HSL for WBG-PSCs should be highly wettable to the perovskite precursor solution, favorable for high-quality perovskite crystallization, capable of passivating the defects near the buried interface and energy level well-matched with the valance band of WBG perovskites [28]. Recently, we demonstrated the successful application of a cyanovinyl phosphonic acid (CPA)-based hole-selective material (HSM), i.e., (2-(4-(bis(4-methoxyphenyl)amino)-phenyl)-1-cyanovinyl)phosphonic acid (MPA-CPA), in p-i-n PSCs [28]. Upon forming a bilayer stack of a chemically anchored self-assembled monolayer plus an unadsorbed overlayer, a superwetting environment is created for perovskite deposition and enables high-quality perovskite thin films with minimized defects at the buried interface. Eventually, PSCs with E_g of 1.56 eV achieved a PCE of 25.4% and PSCs with E_g of 1.68 eV achieved a surprising V_{OC} of 1.24 V.

In this work, we constructed a series of CPA-based molecular HSMs by varying substituents on the triphenylamine group, namely (2-(4-(bis(4-methyl)amino)phenyl)-1-cyanovinyl)phosphonic acid (MePA-CPA), (1-cyano-2-(4-(di-*p*-tolylamino)phenyl)vinyl)phosphonic acid (TPA-CPA), and MPA-CPA. On the indium tin oxide (ITO) substrate, these molecules dynamically formed self-assembled layers, containing a surface adsorbed layer and an unabsorbed overlayer, to which we refer as a bilayer for convenience. This bilayer structure improves the wetting and interfacial properties of the ITO substrate, resulting in the formation of a highly crystalline perovskite film with less defects [28]. Compared with MPA-CPA and TPA-CPA, the MePA-CPA showed a more suitable highest occupied molecular orbital (HOMO) energy level and thus improved energetic alignment with the 1.68 eV perovskite. As a result, the MePA-CPA-based WBG-PSC achieved a high PCE of 22.3% and a best V_{OC} of 1.29 V, representing the lowest V_{OC}-deficit (0.39 V) among WBG-PSCs. Moreover, the bilayer stack on ITO substrate is found to improve the stability of WBG-PSCs. The unadsorbed molecules can be dissolved into perovskite precursor solution, which stay in the formed perovskite layer, playing a role on defect passivation and suppressing halide segregation. As a result, the MePA-CPA-based WBG perovskite devices maintain ~90% of its initial PCE value after 800 h in operating with controlled atmosphere humidity (relative humidity (RH) ~40%) and stable temperature at ~45 °C.

2 Experimental

2.1 Materials

Patterned ITO (~10 Ω sq^{-1}) coated glass was purchased from Beijing HuaMin New Materials Technology Co., Ltd. (China). Quartz substrate, formamidine hydroiodide (FAI), and lead iodide (PbI_2) were sourced from Advanced Election Technology Co., Ltd. (China). Lead bromide ($PbBr_2$) was obtained from Energy Chemical (China). Cesium iodide (CsI) was acquired from Shanghai Macklin Biochemical Technology Co., Ltd. (China). Methylamine hydrobromide (MABr) and 2-phenylethylamine hydroiodide (PEAI) were purchased from Xi'an Yuri Solar Co., Ltd. (China). Fullerene (C_{60}) was sourced from Nanjing/Jiangsu XFNANO Materials Tech Co., Ltd. (China). Bathocuproine (BCP) was obtained from Tokyo Chemical Industry (Japan). All the anhydrous solvents were procured from Acros Organics (Belgium). 4-[*N*,*N*-Di(*p*-tolyl)amino]benzaldehyde and 2-diethoxyphosphorylacetonitrile were purchased from Shanghai Haohong Scientific Co., Ltd. (China). Bromotrimethylsilane (TMSBr) was sourced from Tokyo Chemical Industry (Japan). All materials were utilized without further treatment.

2.2 WBG-PSC fabrication

The ITO glasses underwent a sequential cleaning process involving soapy water, deionized water, ethanol, and acetone. Subsequently, the substrates were subjected to a 15-min treatment with ultraviolet (UV) ozone before film fabrication. For the deposition of HSLs, solutions of MPA-CPA, MePA-CPA, and TPA-CPA at a concentration of 1.0 mg mL^{-1} in anhydrous ethanol were used. The CPA-based HSMs solutions were spin-coated onto the glass/ITO substrates at 3,000 r min^{-1} for 30 s, followed by annealing at 100 °C for 10 min. The perovskite precursor solution ($Cs_{0.05}FA_{0.80}MA_{0.15}Pb(I_{0.75}Br_{0.25})_3$) was prepared by mixing CsI, MABr, FAI, PbI_2, and $PbBr_2$ in *N*,*N*-dimethylformamide (DMF) and dimethyl sulfoxide (DMSO) mixed solvent (DMF:DMSO volume-ratio being 4:1). The solution was stirred at 60 °C for 12 h. Subsequently, 75 μL of the perovskite precursor solution was spin-coated onto the HSL using a two-step spin-coating procedure. The first step involved spinning at 2,000 r min^{-1} for 10 s, followed by the

second step at 6,000 r min^{-1} for 40 s. At 25 s into the second step, 200 μL of chlorobenzene was slowly dripped onto the film. The resulting perovskite film was annealed at 100 °C for 30 min. A solution of PEAI in isopropanol (IPA) with a concentration of 1 mg mL^{-1} was spin-coated at 6,000 r min^{-1} for 30 s without subsequent annealing. After the deposition of the passivation layer, 20 nm C_{60}, 7 nm BCP, and 100 nm silver (Ag) electrode were thermally evaporated.

2.3 Characterization

Current density-voltage (*J-V*) characteristics of WBG-PSCs were measured using a Keithley 2400 Source Meter under xenon lamp with simulated AM 1.5G solar illumination condition (Zolix Instrument Co., Ltd., China). The light intensity was calibrated to 100 mW cm^{-2} by standard silicon cell prior to testing. The *J-V* scans for WBG-PSCs were conducted in both forward and reverse sweep modes, spanning voltage ranges from −0.1 to 1.32 V and from 1.32 to −0.1 V, respectively, with a scan step of 0.02 V (or 0.01 V) and a delay time of 100 ms. The active area of the small-area devices was defined using a metal aperture, resulting in an active area of 0.0805 cm^2 (while the device contact area remained at 0.13 cm^2). Stabilized power output measurements of the devices were obtained by maintaining a constant voltage near the maximum power point (MPP) (V_{MPP}) and recording the corresponding current output under illumination. V_{MPP} was determined from the MPP of the *J-V* curves. External quantum efficiency (EQE) measurements were conducted using SCS600 Solar Cell Quantum Efficiency Measurement System (Zolix Instrument Co., Ltd., China) with a xenon arc lamp. The system was calibrated using a silicon reference cell with a known spectral response before measurement. Operational stability assessments were carried out by placing the devices within the nitrogen chamber subjected to continuous white light-emitting diodes (LED) illumination (equal to 1 sun intensity), under controlled humidity (30%–45% RH) condition. The MPP tracking was executed based on reverse scans every 12 h. For electroluminescence (EL) measurements, a bias voltage of 2.0 V was applied to the WBG-PSCs. Subsequently, EL images were captured using an industrial charge coupled device (CCD) camera (Mindvision Technology Co., Ltd., China) with a prime lens.

3 Results and discussion

3.1 Tuning molecular energy levels and characterization of WBG perovskite films

Previously, we have demonstrated that spin-coating a high concentration solution (~1 mg mL^{-1}) of HSMs with anchoring groups would form a bilayer structure on ITO substrate [28], as shown in Figure 1a. The molecules in the bottom layer are immobilized by forming covalent bonds with the substrate while the ones in the upper layer are disordered. The energetic alignments between WBG perovskite and HSLs are essential for improving the photovoltaic performance [27]. To match the valence band of WBG perovskite, we adjusted the HOMO energy levels of HSMs by using different substituents (OMe, Me, and H, with varied electron-donating capability) on the triphenylamine group. The molecular structures of MPA-CPA, MePA-CPA, and TPA-CPA are shown in Figure 1b, with the synthesis and characterization details in the Supplementary Information. Their E_g and molecular energy levels (Table S1, Supporting Information online) were estimated from UV-visible (UV-vis) absorption spectra and cyclic voltammetry (CV) measurements (Figure S1). Figure 1c displays the energy level alignment of MPA-CPA, MePA-CPA, and TPA-CPA relative to the 1.68 eV perovskite. The HOMO energy levels of MePA-CPA (−5.59 eV) are closer to the valence band of WBG perovskite (−5.64 eV) than those of MPA-CPA (−5.46 eV) and TPA-CPA (−5.71 eV), suggesting a more suitable energetic alignment between MePA-CPA and WBG perovskite. Considering that the final state of HSL in WBG-PSCs contains self-assembled monolayer only, we further evaluated the energy levels of CPA-based HSMs in thin-film state with DMF washing. Figure S2 (Supporting Information online) shows the UV photoelectron spectroscopy (UPS) of CPA-based HSMs, showing similar results with the CV measurement.

The composition of WBG perovskite used in this work is $Cs_{0.05}FA_{0.80}MA_{0.15}Pb(I_{0.75}Br_{0.25})_3$ (FA is formamidinium and MA is methylammonium), which presents a bandgap of 1.68 eV (Figure S3). The perovskites were deposited on MPA-CPA, MePA-CPA, and TPA-CPA by a one-step anti-solvent method. The terminal ends of the HSMs slightly affect their wetting and interfacial properties. Compared with MPA-CPA and TPA-CPA, the wettability of perovskite solution on methyl group ended MePA-CPA slightly decreased, while it does not sacrifice the coverage and uniformity of perovskite films (Figure S4). The crystallinity and morphology of the perovskite films remain similar on all three CPA-based HSMs, as confirmed by X-ray diffraction (XRD) (Figure 1d) and top-view scanning electron microscopy (SEM) images (Figure S5). As a result, the absorption spectra of perovskite films are also the same (Figure S6). The bottom surface of perovskite films was exposed by peeling off using an epoxy encapsulant and observed by SEM [29]. All samples show very similar morphology and grain size without apparent pinholes and cracks at the bottom surface (Figure 1e–g). Therefore, we concluded that our molecular engineering strategy did not change the crystallization and film morphological quality of WBG perovskite films.

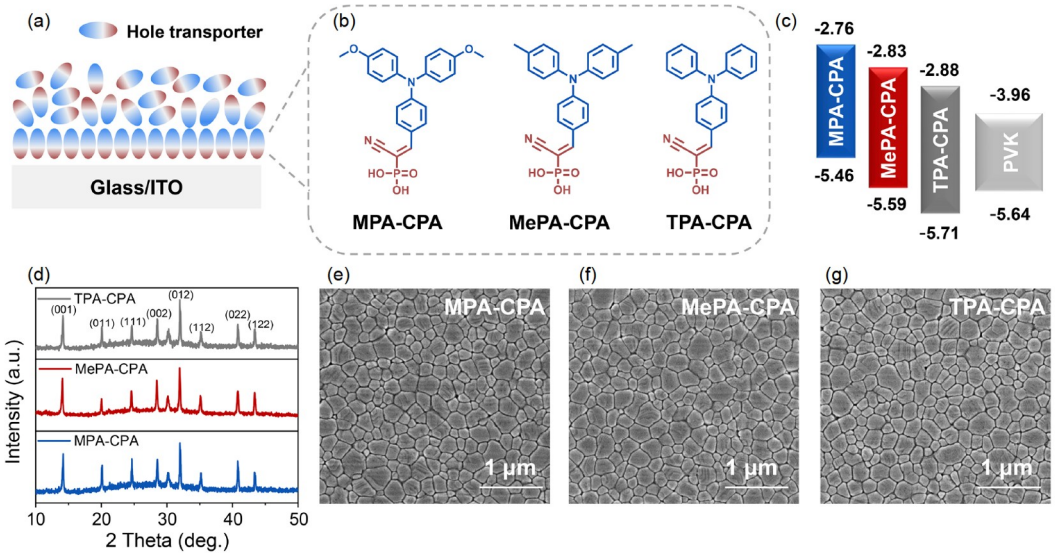

Figure 1 Molecular HSMs and perovskite films. (a) Schematic diagram of bilayer stack of CPA-based molecules on Glass/ITO substrate. (b) Molecular structures of MPA-CPA, MePA-CPA, and TPA-CPA. (c) Energetic diagram of perovskite and the molecular HSMs. (d) XRD patterns of WBG perovskite films deposited on MPA-CPA, MePA-CPA, and TPA-CPA. (e–g) SEM images of the bottom surface of WBG perovskite films deposited on different HSMs (color online).

3.2 Energy level alignment improving photovoltaic performance of WBG-PSCs

The MPA-CPA, MePA-CPA, and TPA-CPA were applied for fabricating WBG-PSCs with a device structure of ITO/HSL/perovskite/PEAI/C_{60}/BCP/Ag. We preliminarily optimized the spin-coating concentration of these HSMs (0.5, 1, 2, 3 mg mL^{-1} in ethanol), and found that a solution with a concentration of 1 mg mL^{-1} realized the optimal photovoltaic performance (Figure S7). Figure 2a shows the typical current density-voltage (*J*-*V*) curves of devices based on the three CPA-based HSLs, and the relevant photovoltaic parameters are listed in Table S2. The short-circuit current density (J_{SC}) of these devices was almost identical, with values around 21 mA cm^{-2}, suggesting an excellent hole extraction and transportation capability of these CPA-based HSLs at least at short-circuit state (Figure S8). These results coincident well with the EQE curves of the devices (Figure 2b), also suggesting negligible parasitic absorption of the molecular hole-transporters (Figure S9). The integrated J_{SC} values are 20.83, 20.88, and 20.61 mA cm^{-2} for MPA-CPA, MePA-CPA, and TPA-CPA-based devices, respectively. By contrast, the V_{OC} parameters were highly dependent on the HSLs. The methoxyl substituted MPA-CPA-based devices exhibited an average V_{OC} of 1.24 V, which agrees with our previously reported results (Table S3). The unsubstituted TPA-CPA-based devices showed a lower average V_{OC} of 1.22 V, which might be related to its deep HOMO energy level and will be discussed later. Surprisingly, the methyl substituted MePA-CPA-based devices achieved an unprecedentedly average V_{OC} of 1.28 V, with the champion value over 1.29 V (Figure 2c). Accordingly, the MePA-CPA-based devices achieved higher PCEs (>22%) than those of MPA-CPA (~21%) and TPA-CPA (20%)-based devices (Figure S8). We note that these devices show negligible hysteresis effect during the *J*-*V* curves measurement (Figure S10). Figure S11 shows the steady-state PCEs of these devices, further confirming the performance improvement contributed by the modulation of HSMs. Furthermore, MePA-CPA-based devices showed higher PCE compared with ([2-(9*H*-carbazol-9-yl) ethyl] phosphonic acid) (2PACz), which is the most frequently used as HSM in WBG-PSCs (Figure S10).

The relatively large V_{OC}-deficit is a common challenge among WBG-PSCs, which severely restricts their PCE improvement. Based on literature survey, we collected the V_{OC} of almost all high-performance WBG-PSCs with E_g between 1.65–1.70 eV, and found that most devices show V_{OC} lower than 90% of their SQ limit (Figure 2d, with details listed in Table S4), which have V_{OC}-deficits larger than 0.40 V [6,8,19,21,23,24,27,30–44]. Here, our MePA-CPA-based 1.68 eV WBG-PSC achieved the highest V_{OC} of 1.29 V, realizing a V_{OC}-deficit of 0.39 V, which is the smallest V_{OC}-deficit among WBG-PSCs with similar E_g to the best of our knowledge. We expect that the strategy developed in this work for achieving high V_{OC} is highly useful and transferable to the perovskite-involved tandem technologies.

As the hole extraction and transportation of these HSLs are very similar as mentioned above, the improvement in V_{OC} should be highly related to the non-radiative recombination processes. To quantify the contributions of non-radiative recombination, we measured the EL spectra (Figure S12) of

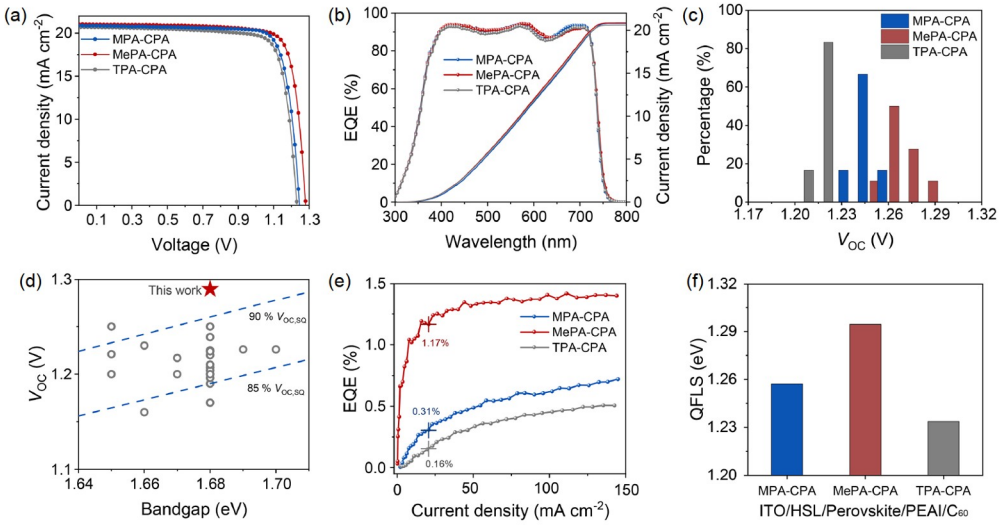

Figure 2 The performance of WBG devices deposited on different HSMs. (a) Typical *J*-*V* curves of WBG perovskite devices deposited on different HSMs. (b) EQE curves of WBG-PSCs deposited on MPA-CPA, MePA-CPA, and TPA-CPA, with integrated J_{SC} values of 20.83, 20.87, and 20.61 mA cm^{-2}. (c) Histograms of V_{OC} in WBG perovskite devices. (d) Summary of reported V_{OC} with bandgap around 1.68 eV in WBG-PSCs. The value of this work is highlighted with a star. (e) EQE_{EL} of WBG perovskite devices deposited on different HSMs. (f) QFLS for the ITO/HSL/1.68 eV perovskite/PEAI/C_{60} samples calculated from their PLQY values (color online).

these WBG-PSCs by operating them as LEDs. The EQE of EL can be applied to calculate the non-radiative recombination V_{OC} loss, called ΔV_3 (Figure 2e) [45]. The ΔV_3 can be calculated using the equation: $\Delta V_3=\frac{kT}{q}\ln(EQE_{EL})$, where k is the Boltzmann constant (k = 1.380649 × 10^{-23} J K^{-1}). We can extract the EQE_{EL} at an injection current density around 20.70 mA cm^{-2} (the J_{SC} of devices worked as solar cells) to be 1.17%, 0.31%, and 0.16% for MePA-CPA, MPA-CPA, and TPA-CPA-based devices, respectively. Accordingly, the ΔV_3 calculated by the equation are 114, 148, and 165 mV, respectively. The calculated results and correlative data are listed in Table S5. The lower value of ΔV_3 of MePA-CPA-based device indicates the effective suppression of non-radiative recombination in perovskite, which minimizes the non-radiative recombination loss to 0.11 V, and thus obtains a higher V_{OC}. We estimated the pseudo-*J*-*V* (p-*JV*) curves using the measured *J*-*V* scan from EL, and the corresponding curves are shown in Figure S13. In the absence of transport losses, the p-V_{OC} and p-fill factor (p-FF) of full cells based on MePA-CPA are higher than cells based on MPA-CPA and TPA-CPA, which is in accordance with the *J*-*V* curves (Table S6).

We further utilized quasi-Fermi level splitting (QFLS) estimated from photoluminescence quantum yield (PLQY) results to quantify the V_{OC} potential for every individual stack (Figure S14). The calculated QFLS for ITO/HSLs/1.68 eV perovskite/PEAI half stacks, and ITO/HSLs/1.68 eV perovskite/PEAI/C_{60} complete stacks are shown in Figure 2f and Figure S15, with relevant parameters concluded in Table S7. The perovskites deposited on MePA-CPA exhibit higher QFLS values in both half and full stacks compared with those of MPA-CPA and TPA-CPA, and the higher QFLS might be explained by improved energetic alignment, as schematically demonstrated in Figure S16 [46]. The HOMO energy level of MePA-CPA was closer to the valence band of perovskite when compared with that of MPA-CPA, resulting in larger QFLS values in the complete stack and in agreement with the highest V_{OC} of MePA-CPA-based devices. The unmatched energetic alignment between TPA-CPA and WBG perovskite impedes the injection of holes in operating, resulting in lower V_{OC} parameter. Moreover, the perovskite films deposited on MePA-CPA showed the longest Shockley-Read-Hall (SRH) lifetime (τ_{SRH} = 7.6 μs) (Figure S17) and the highest PL intensity (Figure S18) among those of CPA-based HSMs. Considering very similar molecular structures and perovskite morphology as well as crystallinity, the interfacial recombination process should be the major difference caused by the three CPA-based materials. As a result, the MePA-CPA realized improved energetic alignment and reduced interfacial recombination in perovskite films, leading to the high performance of WBG-PSCs, especially the unprecedented V_{OC} in 1.68 eV WBG-PSCs.

3.3 Penetrated CPA molecules suppressing halide segregation in WBG perovskites

As shown in the first panel of Figure 3a, the spin-coated MePA-CPA (1 mg mL^{-1}) led to a bilayer structure on ITO. When directly depositing perovskite films on such bilayer structure, the unadsorbed MePA-CPA molecules could be dissolved into the perovskite precursor solution because of its high solubility in DMF/DMSO mixed solvent (Figure S19). Therefore, part of the dissolved CPA-based molecules

will penetrate into the perovskite layer, mainly embed at grain boundaries due to its large molecular size. The penetrated CPA-based molecules have been demonstrated to passivate the interstitial lead (Pb_i) and lead-iodide antisite (Pb_I) defects in our previous work [28]. Here, to get an insight into the effect of the unadsorbed molecules in the bilayer structure on morphology and phase stability of WBG perovskites, we intentionally washed the bilayer structure by blank solvent (mixed DMF/DMSO) before perovskite deposition (Figure 3a), leaving only the chemically adsorbed self-assembled monolayer (SAM) on ITO substrate. We refer to perovskite films deposited on bilayer structure as "target" perovskite, and those deposited on SAM as "control" perovskite. The deposition of perovskite on bilayer structure is easier than that on SAM owing to improved wetting and spreading of perovskite precursor on the former (Figure S20) [26,47], while the grain size of the target and control perovskites are similar (Figure S21).

Under light irradiation, phase segregation commonly happened in mixed-halide perovskites with high molar ratio (>20%) of bromine (Br), which is a challenge in WBG-PSCs [48]. The halide ions generally migrate along grain boundaries and separate into iodide-rich (I-rich) phases and bromide-rich (Br-rich) phases [8]. As the CPA group of penetrated molecules was confirmed to passivate grain boundaries of perovskite by strong chemical chelation, we expect that the penetrated CPA-based molecules could suppress the halide segregation in WBG perovskite and improve their photostability.

To prove this expectation, the target and control perovskite samples were exposed to 1-sun equivalent illumination in air (RH ~50%, ~22 °C) for 20 min, during which their PL spectra and XRD patterns were tracked. As shown in Figure 3b, c, initially both samples showed a PL peak at 740 nm (blue curves). As the illumination time increased, the PL peak of control perovskite broadened at the long wavelength side, with peak wavelength red-shifted from 740 to 750 nm (Figure 3c), suggesting the formation of low bandgap I-rich component. On the contrary, the PL peak of the target perovskite is much less changed. Figure S22 shows the XRD patterns of target and control perovskite films before and after light soaking. After light irradiation for 6 h, the 2θ of (001) (002) (012) peaks of the control sample shifted by 0.33°, whereas those of the target perovskite are much less shifted, suggesting the formation of I-rich phase in mixed halide perovskite [48]. Both PL and XRD results indicate that WBG perovskite films deposited on bilayer structure show higher photostability than that on SAM. To further verify that the improved phase stability on bilayer structure which related to the penetrated MePA-CPA, we fabricated another set of MePA-CPA-added perovskite films *via* intentionally adding a low concentration of MePA-CPA (10^{-4} mg mL^{-1}) into the perovskite precursor solution as an additive. As shown in Figure S23, the photostability was also improved upon WBG perovskite adding MePA-CPA, confirming the positive effect of penetrated CPA-based molecules on the photostability of WBG perovskites.

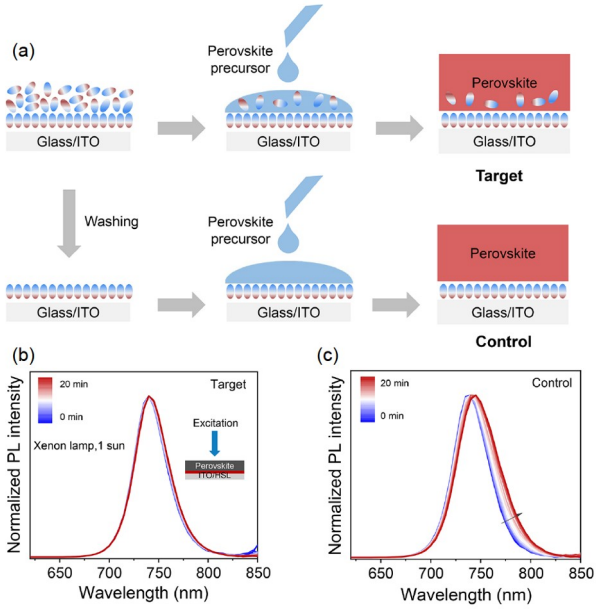

Figure 3 Impact of the bilayer structure on phase stability of WBG perovskite films. (a) Schematic description of the deposition of perovskite thin-films on bilayer and SAM. The unadsorbed CPA-based molecules in bilayer structure will partly be penetrated into the perovskite layer. Evolution of steady-state PL spectra for the target (b) and control (c) perovskite films under light irradiation (xenon lamp, 1 sun) for 20 min (color online).

3.4 Bilayer structure improving reproducibility and stability of WBG-PSCs

We further compared reproducibility and stability of WBG-PSCs based on the target and control perovskite films. As shown in Figure 4a, b and Figure S24, the distribution of PCE values in target devices (22.0% ± 0.3%) is narrower than that of control devices (20.7% ± 0.8%), resulting from the narrower distribution of V_{OC} (1.27 ± 0.01 V for target devices, 1.25 ± 0.02 V for control devices) and FF (82.5% ± 2.0% for target devices, 80.4% ± 2.2% for control devices) values. We also tried to add some MePA-CPA as additives into perovskite precursor solution, and found that the resulting device performance is similar to that of depositing perovskites on the bilayer HSL (Figure S25). The improved reproducibility in target WBG-PSCs was caused by the improved wettability of bilayer structure and enhanced deposition of perovskite films. Such improved wettability is also beneficial to the fabrication of large area device (Figure S20). As a demonstration, we have fabricated large-area WBG-PSCs with active area larger than 1 cm^2. Figure 4c shows *J-V* curves of the champion 1 cm^2 device that achieved a promising PCE of 21.46% with V_{OC} of 1.28 V.

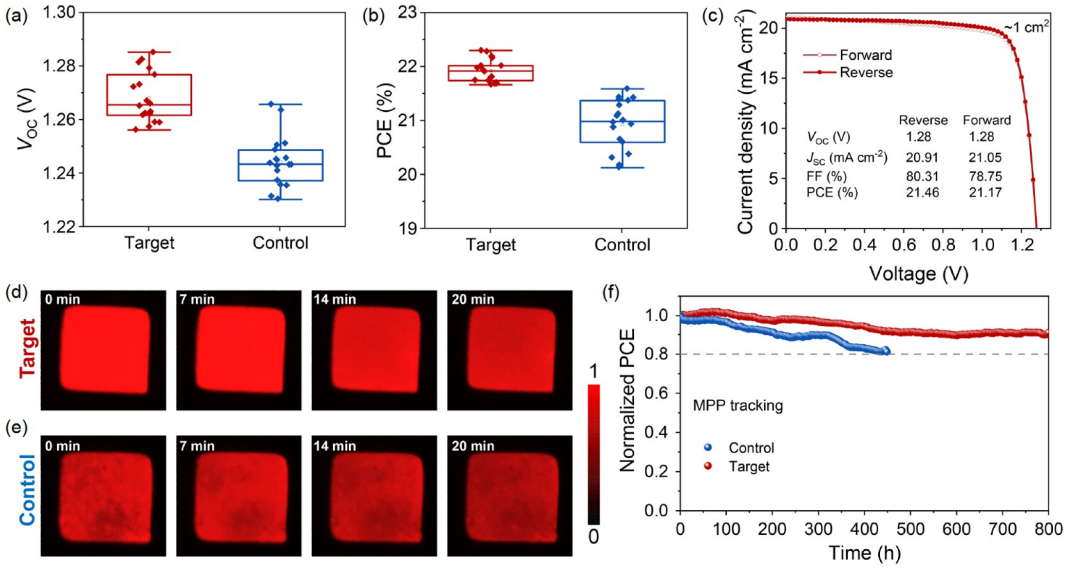

Figure 4 Reproducibility and stability of WBG-PSCs. Statistics of V_{OC} (a) and PCE (b) values obtained from *J-V* characteristic in reverse sweep modes for WBG-PSCs based on target and control perovskites. (c) *J-V* curves of the champion WBG-PSC with an aperture area over 1 cm^2. EL mapping of target (d) and control (e) perovskite-based WBG-PSCs under 2.0 V forward bias for 20 min. The area of the luminous region is 0.065 cm^2. The scale bar represents the normalized EL intensity of devices. (f) Operational stability of WBG-PSCs in nitrogen condition (color online).

The small PCE gap between ~0.1 and 1 cm^2 devices, as well as the very high V_{OC} performance suggests that the new HSM of MePA-CPA and the unique bilayer structure are promising for future application in perovskite/silicon tandem solar cells.

As mentioned above, the inclusion of CPA-based molecules in perovskite layer improves photostability of mixed-halide WBG perovskite films by suppressing halide migration and segregation. The halide segregation is prone to happening in mixed-halide perovskite films with large amount of charge carriers, either through photoexcitation or current injection [48], and EL mapping is a more straightforward method as uniformity change of the films can be directly observed by naked eyes. We thus further evaluated the phase stability of WBG perovskite in complete devices under electric field by EL mapping. When a forward bias of 2.0 V external voltage was applied to the devices, the target perovskite-based devices showed a bright and homogeneous EL over the whole working area, while the intensity and uniformity of EL image for the control perovskite-based devices are inferior (Figure 4d, e). Moreover, the EL of the latter decreased faster than the former, in both terms of intensity and uniformity. These results further suggest that the passivation of perovskite by CPA-based molecules at grain boundaries effectively enhanced the phase stability of WBG-PSCs by suppressing halide migration.

We further explored the operational stability of WBG-PSCs based on target and control perovskites by using MPP tracking under accelerated aging conditions based on the International Summit on Organic Photovoltaic Stability (ISOS) [49]. The typical *J-V* curves of control and target devices are shown in Figure S26. Under continuous illumination (white LED with equal to 1 sun intensity) with controlled atmosphere humidity (RH ~40%) and temperature (~45 °C), the target perovskite-based devices maintained 90% of their initial PCE value after ~800 h. By contrast, the control perovskite-based devices only retain 80% of their initial performance after ~450 h under the same testing condition (Figure 4f, Figure S27). The corresponding photovoltaic parameters are shown in Figure S28. The improved operational stability of target device was consistent with the suppression of halide segregation in target perovskite, demonstrating that bilayer structure remarkably improves the stability of mixed-halide WBG devices. In addition, we conducted the heat stability test at 85 °C. The devices retained ~90% of their initial performance for 120 h, as shown in Figure S29.

4 Conclusions

We have synthesized a series of CPA-featured amphiphilic HSMs and investigated their application in WBG-PSCs. Upon spin-coating, the CPA-based molecules dynamically formed a bilayer stack on the ITO substrate, which contains a chemically anchored layer and an unadsorbed overlayer. The bilayer structure not only favors the wetting and spreading of perovskite precursor solution for achieving homogeneous formation of the perovskite thin films, but also results in penetration of part of CPA-based molecules into the perovskite layer, which improves the phase stability of WBG perovskites by passivating grain boundary defects and sup-

pressing halide segregation. Furthermore, the improved energy level alignment between MePA-CPA and WBG perovskite realized the highest performance of WBG-PSCs. Taking these advantages, MePA-CPA-based WBG-PSCs delivered a highest V_{OC} of 1.29 V and a lowest V_{OC}-deficit of 0.39 V, which is the best result among WBG-PSCs with bandgap in the range of 1.65–1.70 eV. Moreover, the high-performance devices exhibited improved operational stability, mainly arising from the suppression of halide segregation. This work uncovers the underlying mechanism of how CPA-based amphiphilic molecular HSMs improves V_{OC} and stability of WBG-PSCs and provides a universal effective approach to decreasing the V_{OC}-deficit in WBG-PSCs, and also confirms the importance of energy level alignment at the charge-selective layers in PSCs.

Acknowledgements This work was supported by the National Natural Science Foundation of China (22179037), Shanghai pilot program for Basic Research (22TQ1400100-1), Shanghai Municipal Science and Technology Major Project (2018SHZDZX03, 21JC1401700), the Programmer of Introducing Talents of Discipline to Universities (B16017), and the Fundamental Research Funds for the Central Universities. Yue Hu acknowledges support from Royal Society of Chemistry (R23-0749928359). We thank the Research Center of Analysis and Test of East China University of Science and Technology (ECUST); Prof. Yan Li and Mr. Zhuohan Lin from ECUST for EL measurement, Mrs. Mengjing Li from Shiyanjia Lab (www.shiyanjia.com) for the UPS measurement.

Conflict of interest The authors declare no conflict of interest.

Supporting information The supporting information is available online at http://chem.scichina.com and http://link.springer.com/journal/11426. The supporting materials are published as submitted, without typesetting or editing. The responsibility for scientific accuracy and content remains entirely with the authors.

1 Park J, Kim J, Yun HS, Paik MJ, Noh E, Mun HJ, Kim MG, Shin TJ, Seok SI. *Nature*, 2023, 616: 724–730
2 Zhao Y, Ma F, Qu Z, Yu S, Shen T, Deng HX, Chu X, Peng X, Yuan Y, Zhang X, You J. *Science*, 2022, 377: 531–534
3 Chen H, Maxwell A, Li C, Teale S, Chen B, Zhu T, Ugur E, Harrison G, Grater L, Wang J, Wang Z, Zeng L, Park SM, Chen L, Serles P, Awni RA, Subedi B, Zheng X, Xiao C, Podraza NJ, Filleter T, Liu C, Yang Y, Luther JM, De Wolf S, Kanatzidis MG, Yan Y, Sargent EH. *Nature*, 2023, 613: 676–681
4 He R, Wang W, Yi Z, Lang F, Chen C, Luo J, Zhu J, Thiesbrummel J, Shah S, Wei K, Luo Y, Wang C, Lai H, Huang H, Zhou J, Zou B, Yin X, Ren S, Hao X, Wu L, Zhang J, Zhang J, Stolterfoht M, Fu F, Tang W, Zhao D. *Nature*, 2023, 618: 80–86
5 Mariotti S, Köhnen E, Scheler F, Sveinbjörnsson K, Zimmermann L, Piot M, Yang F, Li B, Warby J, Musiienko A, Menzel D, Lang F, Keßler S, Levine I, Mantione D, Al-Ashouri A, Härtel MS, Xu K, Cruz A, Kurpiers J, Wagner P, Köbler H, Li J, Magomedov A, Mecerreyes D, Unger E, Abate A, Stolterfoht M, Stannowski B, Schlatmann R, Korte L, Albrecht S. *Science*, 2023, 381: 63–69
6 Chen B, Chen H, Hou Y, Xu J, Teale S, Bertens K, Chen H, Proppe A, Zhou Q, Yu D, Xu K, Vafaie M, Liu Y, Dong Y, Jung EH, Zheng C, Zhu T, Ning Z, Sargent EH. *Adv Mater*, 2021, 33: 2103394
7 Guo H, Fang Y, Lei Y, Wu J, Li M, Li X, Cheng HB, Lin Y, Dyson PJ. *Small*, 2023, 19: 2302021
8 Isikgor FH, Furlan F, Liu J, Ugur E, Eswaran MK, Subbiah AS, Yengel E, De Bastiani M, Harrison GT, Zhumagali S, Howells CT, Aydin E, Wang M, Gasparini N, Allen TG, Rehman A, Van Kerschaver E, Baran D, McCulloch I, Anthopoulos TD, Schwingenschlögl U, Laquai F, De Wolf S. *Joule*, 2021, 5: 1566–1586
9 Su C, Wang R, Tao J, Shen J, Wang D, Wang L, Fu G, Yang S, Yuan M, He T. *J Mater Chem A*, 2023, 11: 6565–6573
10 Wang R, Li M, Ma Z, He Z, Dong Y, Zhang Y, Xu Z, Su G, Tan Z. *Chem Commun*, 2023, 59: 6255–6258
11 Hang P, Kan C, Li B, Yao Y, Hu Z, Zhang Y, Xie J, Wang Y, Yang D, Yu X. *Adv Funct Mater*, 2023, 33: 2214381
12 Zhao Y, Wang C, Ma T, Zhou L, Wu Z, Wang H, Chen C, Yu Z, Sun W, Wang A, Huang H, Zou B, Zhao D, Li X. *Energy Environ Sci*, 2023, 16: 2080–2089
13 Li T, Xu J, Lin R, Teale S, Li H, Liu Z, Duan C, Zhao Q, Xiao K, Wu P, Chen B, Jiang S, Xiong S, Luo H, Wan S, Li L, Bao Q, Tian Y, Gao X, Xie J, Sargent EH, Tan H. *Nat Energy*, 2023, 8: 610–620
14 Guan H, Zhang W, Liang J, Wang C, Hu X, Pu D, Huang L, Ge Y, Cui H, Zou Y, Fang G, Ke W. *Adv Funct Mater*, 2023, 33: 2300860
15 Zhang X, Li X, Tao L, Zhang Z, Ling H, Fu X, Wang S, Ko MJ, Luo J, Chen J, Li Y. *Small*, 2023, 19: 2208289
16 Xiang W, Liu SF, Tress W. *Angew Chem Int Ed*, 2021, 60: 26440–26453
17 Mahesh S, Ball JM, Oliver RDJ, McMeekin DP, Nayak PK, Johnston MB, Snaith HJ. *Energy Environ Sci*, 2020, 13: 258–267
18 Wang X, Chen Y, Zhang T, Wang X, Wang Y, Kan M, Miao Y, Chen H, Liu X, Wang X, Shi J, Zhang L, Zhao Y. *ACS Energy Lett*, 2021, 6: 2735–2741
19 Xu J, Boyd CC, Yu ZJ, Palmstrom AF, Witter DJ, Larson BW, France RM, Werner J, Harvey SP, Wolf EJ, Weigand W, Manzoor S, van Hest MFAM, Berry JJ, Luther JM, Holman ZC, McGehee MD. *Science*, 2020, 367: 1097–1104
20 Jiang Q, Tong J, Scheidt RA, Wang X, Louks AE, Xian Y, Tirawat R, Palmstrom AF, Hautzinger MP, Harvey SP, Johnston S, Schelhas LT, Larson BW, Warren EL, Beard MC, Berry JJ, Yan Y, Zhu K. *Science*, 2022, 378: 1295–1300
21 Yang G, Ni Z, Yu ZJ, Larson BW, Yu Z, Chen B, Alasfour A, Xiao X, Luther JM, Holman ZC, Huang J. *Nat Photon*, 2022, 16: 588–594
22 Yang G, Ren Z, Liu K, Qin M, Deng W, Zhang H, Wang H, Liang J, Ye F, Liang Q, Yin H, Chen Y, Zhuang Y, Li S, Gao B, Wang J, Shi T, Wang X, Lu X, Wu H, Hou J, Lei D, So SK, Yang Y, Fang G, Li G. *Nat Photon*, 2021, 15: 681–689
23 Yan N, Gao Y, Yang J, Fang Z, Feng J, Wu X, Chen T, Liu SF. *Angew Chem Int Ed*, 2023, 62: e202216668
24 Liu J, De Bastiani M, Aydin E, Harrison GT, Gao Y, Pradhan RR, Eswaran MK, Mandal M, Yan W, Seitkhan A, Babics M, Subbiah AS, Ugur E, Xu F, Xu L, Wang M, Rehman A, Razzaq A, Kang J, Azmi R, Said AA, Isikgor FH, Allen TG, Andrienko D, Schwingenschlögl U, Laquai F, De Wolf S. *Science*, 2022, 377: 302–306
25 Lin Y, Chen B, Zhao F, Zheng X, Deng Y, Shao Y, Fang Y, Bai Y, Wang C, Huang J. *Adv Mater*, 2017, 29: 1700607
26 Al-Ashouri A, Magomedov A, Roß M, Jošt M, Talaikis M, Chistiakova G, Bertram T, Márquez JA, Köhnen E, Kasparavičius E, Levcenco S, Gil-Escrig L, Hages CJ, Schlatmann R, Rech B, Malinauskas T, Unold T, Kaufmann CA, Korte L, Niaura G, Getautis V, Albrecht S. *Energy Environ Sci*, 2019, 12: 3356–3369
27 Al-Ashouri A, Köhnen E, Li B, Magomedov A, Hempel H, Caprioglio P, Márquez JA, Morales Vilches AB, Kasparavicius E, Smith JA, Phung N, Menzel D, Grischek M, Kegelmann L, Skroblin D, Gollwitzer C, Malinauskas T, Jošt M, Matič G, Rech B, Schlatmann R, Topič M, Korte L, Abate A, Stannowski B, Neher D, Stolterfoht M, Unold T, Getautis V, Albrecht S. *Science*, 2020, 370: 1300–1309
28 Zhang S, Ye F, Wang X, Chen R, Zhang H, Zhan L, Jiang X, Li Y, Ji X, Liu S, Yu M, Yu F, Zhang Y, Wu R, Liu Z, Ning Z, Neher D, Han L, Lin Y, Tian H, Chen W, Stolterfoht M, Zhang L, Zhu WH, Wu Y. *Science*, 2023, 380: 404–409
29 Chen S, Dai X, Xu S, Jiao H, Zhao L, Huang J. *Science*, 2021, 373:

902–907
30 Luo X, Luo H, Li H, Xia R, Zheng X, Huang Z, Liu Z, Gao H, Zhang X, Li S, Feng Z, Chen Y, Tan H. *Adv Mater*, 2023, 35: 2207883
31 Xu K, Al-Ashouri A, Peng ZW, Köhnen E, Hempel H, Akhundova F, Marquez JA, Tockhorn P, Shargaieva O, Ruske F, Zhang J, Dagar J, Stannowski B, Unold T, Abou-Ras D, Unger E, Korte L, Albrecht S. *ACS Energy Lett*, 2022, 7: 3600–3611
32 Chen J, Wang D, Chen S, Hu H, Li Y, Huang Y, Zhang Z, Jiang Z, Xu J, Sun X, So SK, Peng Y, Wang X, Zhu X, Xu B. *ACS Appl Mater Interfaces*, 2022, 14: 43246–43256
33 Zheng Y, Wu X, Liang J, Zhang Z, Jiang J, Wang J, Huang Y, Tian C, Wang L, Chen Z, Chen CC. *Adv Funct Mater*, 2022, 32: 2200431
34 Fang Z, Jia L, Yan N, Jiang X, Ren X, Yang S, Liu SF. *InfoMat*, 2022, 4: e12307
35 Liu J, Aydin E, Yin J, De Bastiani M, Isikgor FH, Rehman AU, Yengel E, Ugur E, Harrison GT, Wang M, Gao Y, Khan JI, Babics M, Allen TG, Subbiah AS, Zhu K, Zheng X, Yan W, Xu F, Salvador MF, Bakr OM, Anthopoulos TD, Lanza M, Mohammed OF, Laquai F, De Wolf S. *Joule*, 2021, 5: 3169–3186
36 Kim D, Jung HJ, Park IJ, Larson BW, Dunfield SP, Xiao C, Kim J, Tong J, Boonmongkolras P, Ji SG, Zhang F, Pae SR, Kim M, Kang SB, Dravid V, Berry JJ, Kim JY, Zhu K, Kim DH, Shin B. *Science*, 2020, 368: 155–160
37 Ye JY, Tong J, Hu J, Xiao C, Lu H, Dunfield SP, Kim DH, Chen X, Larson BW, Hao J, Wang K, Zhao Q, Chen Z, Hu H, You W, Berry JJ, Zhang F, Zhu K. *Sol RRL*, 2020, 4: 2000082
38 Lin C-, Lee J, Kim J, Macdonald TJ, Ngiam J, Xu B, Daboczi M, Xu W, Pont S, Park B, Kang H, Kim J-, Payne DJ, Lee K, Durrant JR, McLachlan MA. *Adv Funct Mater*, 2020, 30: 1906763
39 Kim DH, Muzzillo CP, Tong J, Palmstrom AF, Larson BW, Choi C, Harvey SP, Glynn S, Whitaker JB, Zhang F, Li Z, Lu H, van Hest MFAM, Berry JJ, Mansfield LM, Huang Y, Yan Y, Zhu K. *Joule*, 2019, 3: 1734–1745
40 Yang W, Long H, Sha X, Sun J, Zhao Y, Guo C, Peng X, Shou C, Yang X, Sheng J, Yang Z, Yan B, Ye J. *Adv Funct Mater*, 2022, 32: 2110698
41 Wang D, Guo H, Wu X, Deng X, Li F, Li Z, Lin F, Zhu Z, Zhang Y, Xu B, Jen AKY. *Adv Funct Mater*, 2022, 32: 2107359
42 Lin YH, Sakai N, Da P, Wu J, Sansom HC, Ramadan AJ, Mahesh S, Liu J, Oliver RDJ, Lim J, Aspitarte L, Sharma K, Madhu PK, Morales-Vilches AB, Nayak PK, Bai S, Gao F, Grovenor CRM, Johnston MB, Labram JG, Durrant JR, Ball JM, Wenger B, Stannowski B, Snaith HJ. *Science*, 2020, 369: 96–102
43 Liu Z, Zhu C, Luo H, Kong W, Luo X, Wu J, Ding C, Chen Y, Wang Y, Wen J, Gao Y, Tan H. *Adv Energy Mater*, 2023, 13: 2203230
44 Zhu Z, Mao K, Zhang K, Peng W, Zhang J, Meng H, Cheng S, Li T, Lin H, Chen Q, Wu X, Xu J. *Joule*, 2022, 6: 2849–2868
45 Liu J, Chen S, Qian D, Gautam B, Yang G, Zhao J, Bergqvist J, Zhang F, Ma W, Ade H, Inganäs O, Gundogdu K, Gao F, Yan H. *Nat Energy*, 2016, 1: 16089
46 Caprioglio P, Smith JA, Oliver RDJ, Dasgupta A, Choudhary S, Farrar MD, Ramadan AJ, Lin YH, Christoforo MG, Ball JM, Diekmann J, Thiesbrummel J, Zaininger KA, Shen X, Johnston MB, Neher D, Stolterfoht M, Snaith HJ. *Nat Commun*, 2023, 14: 932
47 Roß M, Severin S, Stutz MB, Wagner P, Köbler H, Favin-Lévêque M, Al-Ashouri A, Korb P, Tockhorn P, Abate A, Stannowski B, Rech B, Albrecht S. *Adv Energy Mater*, 2021, 11: 2101460
48 Lim VJY, Knight AJ, Oliver RDJ, Snaith HJ, Johnston MB, Herz LM. *Adv Funct Mater*, 2022, 32: 2204825
49 Khenkin MV, Katz EA, Abate A, Bardizza G, Berry JJ, Brabec C, Brunetti F, Bulović V, Burlingame Q, Di Carlo A, Cheacharoen R, Cheng YB, Colsmann A, Cros S, Domanski K, Dusza M, Fell CJ, Forrest SR, Galagan Y, Di Girolamo D, Grätzel M, Hagfeldt A, von Hauff E, Hoppe H, Kettle J, Köbler H, Leite MS, Liu S, Loo YL, Luther JM, Ma CQ, Madsen M, Manceau M, Matheron M, McGehee M, Meitzner R, Nazeeruddin MK, Nogueira AF, Odabaşı Ç, Osherov A, Park NG, Reese MO, De Rossi F, Saliba M, Schubert US, Snaith HJ, Stranks SD, Tress W, Troshin PA, Turkovic V, Veenstra S, Visoly-Fisher I, Walsh A, Watson T, Xie H, Yıldırım R, Zakeeruddin SM, Zhu K, Lira-Cantu M. *Nat Energy*, 2020, 5: 35–49